RESEARCH PAPER



Ant nest geometry, stability, and excavation-inspiration for tunneling

Meron Belachew¹ • Karie Yamamoto¹ • Elliot Nichols¹ • Danrong Zhang¹ • J. David Frost¹ • Chloé Arson¹

Received: 27 March 2023 / Accepted: 24 October 2023 / Published online: 12 February 2024 © The Author(s), under exclusive licence to Springer-Verlag GmbH Germany, part of Springer Nature 2024

Abstract

Underground construction and tunnel excavation are known to redistribute stresses and cause ground displacement. Analytical solutions for stress distribution typically break down at shallow depths or in soil masses that exhibit high spatial variability, making numerical simulations necessary. Seeking to find new geometries and excavation strategies for underground construction, we propose to look to nature for inspiration. We extract 3D digital twins of Florida Harvester ant (*Pogonomyrmex Badius*) structures from a nest cast in situ and simulate the stress and displacement fields around that nest with the Finite Element Method (FEM). Stress invariants around the main shaft are compared to those around idealized geometric representations of that shaft, i.e., helixes with a fixed pitch angle and a uniform elliptical cross-section. Helical structures made of circular cross-sections and horizontally oriented elliptical cross-sections interact in a way that reduces the risk of tension failure and distributes the shear stress more evenly. One can show that in addition to the extra stability that they offer and the lower risk of tensile or shear failure that they exhibit, helical shafts have the advantage of requiring less power to excavate than straight sub-vertical shafts.

Keywords 3D scanning · Ant nest · Finite Element Method · Tunneling

1 Introduction

In the nineteenth century, the shipworm (*Teredo Navalis*) was used as inspiration for the Thames tunnel, which is where tunnel shielding began [30]. Brunel, the engineer who invented the design and construction scheme, observed that the mollusc uses a cutting shell to excavate

Meron Belachew mbelachew3@gatech.edu

Karie Yamamoto kyamamoto8@gatech.edu

Elliot Nichols enichols9@gatech.edu

Danrong Zhang dzhang373@gatech.edu

J. David Frost david.frost@ce.gatech.edu

Chloé Arson chloe.arson@ce.gatech.edu

Civil and Environmental Engineering, Georgia Institute of Technology, North Ave NW, Atlanta, GA 30332, USA forward at the tunnel face and advances the rest of the body forward periodically. Shield tunneling has evolved significantly in terms of equipment and excavation techniques, leading to self-driving machines that do not require any human intervention [17]. More recently, it was observed that organisms such as ants, worms, and clams deploy significantly more energy-efficient excavation strategies as compared to those employed by human-designed tunneling machines [11, 38]. Researchers have studied the behavior of burrowing organisms in their natural habitats and in laboratory settings to understand the underlying mechanisms of penetration, excavation, locomotion, and underground stability [9-12, 29, 37, 41, 45, 48]. Mechanical models can explain burrowing strategies used by animals, hence making them suitable to emulate in solutions to practical engineering problems. For example, self-burrowing robots inspired by plant roots were prototyped for sensor installation and soil investigation [8, 31, 36]. The aim of this study is to understand the principles of soil mechanics that explain why ant structures are stable and to identify mechanisms that can be applied to improve tunneling techniques.



Biomimicry is an approach to innovation that seeks sustainable solutions to human challenges by emulating nature's strategies, for instance, by reconstructing molecular structures and interfaces, reproducing biophysical phenomena in the laboratory, modeling the mechanisms that originate biodiversity, or taking inspiration from ecosystems and living organisms. Bio-inspired design is either the product of an exploration of natural systems to solve an engineering problem or the result of the opportune application of biological principles to an engineering project. In the former case, the engineering questions are raised first, and biological systems that can ensure specific functions (e.g., support loads, excavate) are sought to address these issues. In the latter, the biological system is selected first, and an application of the mechanism in that system is sought. In this paper, we follow the second approach, i.e., we select a biological organism that is known to exhibit interesting properties, and we propose mechanical models to enhance our fundamental understanding of these properties and how they impact tunnel advancement strategies. Many applications of biomimicry have been found in bio-inspired geotechnics alone [28]. For example, it is possible to control the resistance to penetration and pullout of an anchor by using snakeskin-inspired interfaces that react differently if displacement is applied in the cranial or caudal direction. More broadly, the importance of anisotropic friction properties for load transfer at the interface between soil and foundation or anchoring elements was noted in several studies that featured new soil/structure interfaces inspired by snakeskin [26, 27, 34, 39, 47]. Similarly, inspiration was taken from the architecture of plant roots to design high-performance deep foundation [1] and anchorage [25] systems. Root pullout resistance was measured by several research teams to support these designs [5, 6, 15, 16]. The fundamental mechanisms of soil/root interaction were studied experimentally in maize, a few days old, [2, 3] and numerically at the scale of a wheat root tip [21].

For convenience and simplicity, human tunneling has mainly been focused on linear alignments that provide the shortest path between two points [13]. The present study aims to find more effective tunneling strategies and alignments by studying underground structures made by ants. The complex structures of subterranean ant nests are not widely known. Biologists have traditionally extracted the geometry of these ant nests using excavation and mapping techniques to generate approximate 2D profile sketches of the nests [22, 40]. After Williams and Lofgren began using dental plaster for nest casting in 1988, Tschinkel continued to expand this field with the casting and extraction of full 3D nest structures of a variety of ant species [44]. Tschinkel observed that the nests of Florida Harvester ants

(Pogonomyrmex Badius) have a particularly unique and interesting geometry with two distinct components, i.e., helical sub-vertical shafts and horizontal chambers [42]. We chose to study Harvester ant nests because of these specific structural features. In this paper, in order to understand why the nests of Harvester ants are stable, we propose to analyze the stress and displacement fields around actual nests as well as simplified nest components. Analytical solutions available to date cannot be applied to complex tunnel structures under biaxial stress such as Harvester ant nests (e.g., see the literature review in [35]). Experimental studies related to ant nests have been limited to small-scale experiments in quasi-2D settings of ant farms that allow observation of the excavation process through a glass panel [11, 29]. No known experimental method has been used to understand the whole three-dimensional mechanical response of the soil around Harvester ant nests. In this study, we thus adopt a numerical approach to model the complex geometry of the ant nests and calculate the stress and displacement fields around the nests. Harvester ant chambers were modeled in 2D with the Discrete Element Method (DEM), and simulations showed that stress redistribution due to arching contributes to the stability of these cavities [13]. 3D DEM models of ant nests were proposed to understand ant excavation strategies and predict the stability of complex ant nest structures [24], but these numerical models have been limited to small portions of the whole nest structure. DEM studies have provided great insight into the mechanical stability of ant nests and have motivated the present study, dedicated to the whole nest structure. Although DEM is a powerful tool for granular mechanics, its computational cost would make it a less desirable choice to model a full nest. Here, we propose an analysis based on the Finite Element Method (FEM).

We begin by modeling an actual ant nest extracted from a site in Florida. We simulate the response of the nest to geostatic stress, and we model idealized portions of that nest, in order to isolate the different mechanisms of structure stability. We present some mechanical conjectures to explain the geometry of Harvester ant nests, and we draw some conclusions for bio-inspired tunneling. Data and methods that pertain to soil characterization, ant nest geometry extraction, mesh generation, and FEM modeling are explained in Sect. 2, which also describes the geometry of the idealized helical shafts that we modeled for benchmarking. The simulation results and their interpretation in light of known analytical solutions are discussed in Sect. 3, which also explains the underlying stability mechanisms. Conclusions on the mechanical functions of the ant nest components and the possible applications to tunnel engineering are presented in Sect. 4.



2 Data and methods

2.1 Soil characterization

2.1.1 Data from the field

The ant nest that is studied here was located in Lee, Florida, in an area that is primarily composed of Blanton sand, a siliceous, fine, clean sand, according to the USGS Web Soil Survey [46]. Of note, the site where the ant nest was extracted was subjected to a full geotechnical index property characterization, which is unique to the present study, since most, if not all, of the literature on ant nest architecture contains no information about the surrounding soil. ASTM standard test methods D 6913, 7263, 2216-19, and 4253/4 were used to obtain the particle gradation, dry unit weight, moisture content, and minimum and maximum void ratios of the soil, respectively. The results of the grain size distribution analysis are summarized in Table 1. The dry unit weight and water content profile were obtained from the field, and because their variability with depth was not significant, average values of γ_{dry} =1.516 g/cm³ and w = 3.287% were used in the subsequent model. The minimum and maximum dry densities of the sand were also measured, and it was found that $\gamma_{drv-min}=1.424$ g/cm³ and $\gamma_{\rm dry-max}$ =1.726 g/cm³.

2.1.2 Soil constitutive model parameters

In the FEM models described in Sect. 2.3, the soil is assigned the Mohr–Coulomb elastoplastic constitutive model, with a non-associate flow rule. The Mohr–Coulomb criterion is chosen for its simplicity and its proven suitability for frictional soil. The method to calculate the Mohr–Coulomb constitutive parameters and the other soil parameters needed to perform the FEM simulations is described below:

(i) Density

By using an average dry density $\gamma_{dry}=1.516g/cm^3$ and water content w=3.287%, we calculate the wet density (total density) of the soil as:

Table 1 Grain size distribution

| D ₆₀ (mm) | D ₃₀ (mm) | D ₁₀ (mm) | D ₅₀ (mm) | C_u | C_c |
|----------------------|----------------------|----------------------|----------------------|-------|-------|
| 0.361 | 0.209 | 0.097 | 0.3 | 3.71 | 1.24 |

The sand falls under the USCS classification SP

$$\gamma_t = \gamma_{\text{dry}}(1+w) = 1.516 \, g/cm^3 (1+0.033)$$

 $\gamma_t = 1.566 \, g/cm^3$

(ii) Young's elastic modulus and Poisson's ratio

The relative density of the soil is used to classify the sand in a spectrum from very loose to very dense, for which typical values of elastic modulus are available in the literature [7]. The relative densities calculated at several depths mainly fall in the loose sand category, for which the Young's modulus can be estimated as E = 20 MPa and the Poisson's ratio as v = 0.3 [7, 14].

(iii) Friction angle

The drained friction angle can be estimated to be about $\phi' = 30^{\circ}$ from empirical correlations by Brinch, Hansen, and Lundgren [33] and from typical values reported in the literature for loose uniform sand [7, 14].

(iv) Cohesion

The sand found in situ was unsaturated. The capillary pressure increases the soil shear strength. In other words, unsaturated sand has an apparent cohesion. This apparent cohesion can be used as the cohesion parameter in the Mohr–Coulomb model [20] to account for the increase in soil shear strength with suction. The apparent cohesion is calculated as a function of the saturation and drained friction parameters of the soil as follows:

$$c'' = c' + \chi(u_a - u_w) \tan \phi' \tag{1}$$

where the effective stress parameter χ is a function of the degree of saturation of the soil, which varies by type of soil. It has been shown that χ could be approximated as the degree of saturation itself for sands [32]. Using the measured data of dry density and moisture content measured in situ, we estimated the saturation degree and, subsequently, the apparent cohesion to be about 6 kPa.

(v) Dilatancy angle

The typical dilatancy angle ψ for loose sand is less than 10° [14]. In the following analyses, we use a value of 10°.

The sand parameters used in the FEM model are summarized in Table 2.

Table 2 Summary of model parameters

| $\gamma_t \text{ (g/cm}^3)$ | E (MPa) | v (-) | $\phi\left(^{o}\right)$ | c (kPa) | $\psi(^{o})$ |
|-----------------------------|---------|-------|-------------------------|---------|--------------|
| 1.566 | 20 | 0.3 | 30 | 6 | 10 |



A parametric study showed that the numerical results were not significantly affected by the values of the elastic modulus, Poisson's ratio, and friction angle of the soil when taken within a range of values typical of a loose sand. However, varying the value of apparent cohesion controlled the onset of plasticity. At very low values of apparent cohesion ($c=1~\mathrm{kPa}$ and $c=0.5~\mathrm{kPa}$), small portions of the domain underwent plastic strains. In the following, we used an apparent cohesion of 6 kPa because it is representative of the in situ conditions.

2.2 Geometry of the ant nest and shafts

2.2.1 Ant nest geometry extracted from the field

The ant nest was molded in place, and the geometric characteristics were measured by using a 3D digital twin of the cast. Various materials such as paraffin wax, dental plaster, and zinc are routinely used to create casts of subterranean ant nests [43]. For the purposes of this study, aluminum was selected because of its low melting point as well as the strength and durability of the cast that is produced after curing.

The casting process used in this study was based on the procedure detailed in [43]. Pure aluminum was heated in a crucible above its melting point of 660.3 °C. The molten aluminum was then poured into the nest opening until the metal began to pool at the surface. The aluminum was left in place until the soil around the nest entrance became cool enough to be handled safely (no longer than 24 h). The cast was extracted from the ground using shovels and hand rakes, and then the remaining soil was washed off with water. After recovering the cast from the field, the next step was to generate a digital replica for use in the subsequent FEM model.

An EinScan Pro HD handheld scanner, developed by Shining 3D, was used to obtain a 3D digital image of the ant nest casts. The scanner uses flash LiDAR to develop an initial raw point cloud of the casting. Before scanning, reflective markers are evenly distributed on the casting. The markers play the role of control points. Markers are read by the scanner first and assigned coordinates. The coordinates of the cloud points that represent the surface of the casting are measured in reference with the coordinates of the markers. The casting needs to have markers placed in a random, nonlinear pattern with at least four markers in each scanning field of view. Therefore, the markers were distributed on the top, bottom, and edges of the ant casting features. The reflectivity of the aluminum made scanning in bright lights difficult; therefore, measures were taken under indirect light, e.g., by holding an umbrella above the casting during the scanning process. The scanner was held by hand and slowly moved around, above, and below the ant nest casting. Point cloud data were collected with a 0.2-mm resolution, meaning each point had no other point within a 0.2 mm radius in any direction. The EXScan Pro software was then used to generate a watertight mesh, such that the surface of the mesh was closed.

2.2.2 Simplified nest geometry for FEM models

The watertight mesh was then pre-processed before being used as a basis to construct the Finite Element mesh. First, the top ~ 17 mm was cut off during the analysis because some overflow had occurred during the field casting process, which led to an excess of aluminum in the top part of the nest. Next, the density of the watertight mesh was reduced in order to allow completion of the FEM simulations within no more than a few days on a workstation, remove ill-shaped elements that would cause convergence issues, and avoid stress concentrations at local geometric irregularities (which would overshadow the results in the rest of the domain). Since the purpose of the study was to understand the effect of the overall nest structure on soil stress distributions, we sought to eliminate the effects of surface roughness. We used Autodesk Meshmixer to remesh the cast into a relatively coarser and more regular mesh, which provided a smoother rendering of the nest geometry, as can be seen in the sample portion shown in Fig. 1.

The gap between the processed mesh and the original mesh was measured along the direction normal to the surface of the processed mesh. The average distance between the smoothed surface and the original surface from the scan, shown in Fig. 2, was found to be 1 mm, which is approximately 10% of the average diameter of the shafts and the average height of the chambers. This deviation was thus judged acceptable to study the overall geometry of the nest excluding the surface roughness of the walls of the ant nest, mainly, the spacing of the chambers, the orientation of the shafts, and the cross-section of the shafts. The mesh densities and nest dimensions before and after pre-processing are summarized in Tables 3 and 4, respectively. In summary, we were able to reduce the overall mesh density by an order of magnitude without compromising on the accuracy of the geometric structure of the nest. Figure 3 shows the post-processed mesh that was used in the Finite Element analysis.

2.2.3 Simplified shaft geometries for FEM models

Figure 4 shows simplified geometries of helical shafts, which are features commonly observed in Florida Harvester ant nests. These models were used for benchmarking against the shafts of the actual nest presented in Sect. 2.2.2



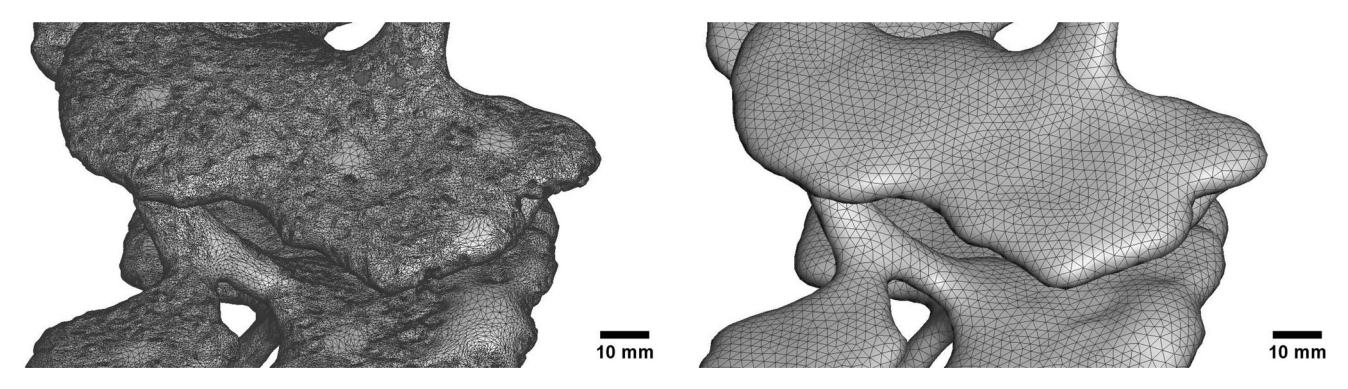


Fig. 1 Sample portion of the cast before (left) and after (right) remeshing

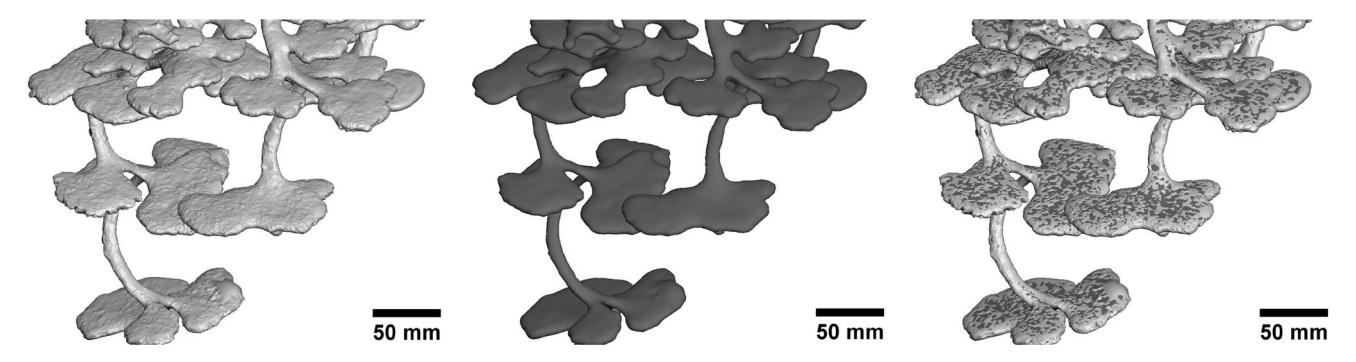


Fig. 2 Originally scanned images (light gray, left), processed images (dark gray, middle), and processed image subtracted from the original image (right)

Table 3 Surface mesh of the ant nest casting before and after processing

| | Vertices | Faces (triangles) |
|------------------|-----------|-------------------|
| As scanned | 1,249,992 | 2,500,076 |
| After processing | 62,439 | 124,950 |

Table 4 Dimensions of the casting before and after processing

| | Height (mm) | Length (mm) | Width (mm) |
|------------------|-------------|-------------|------------|
| As scanned | 450.312 | 399.468 | 342.33 |
| After processing | 432.365 | 397.802 | 340.974 |

and have the geometric features of actual ant shafts, with a helix diameter of 5 cm, pitch angles (θ) between 20° and 70°, and cross-sections that are either circular with a 1 cm diameter or elliptical with major and minor axes of lengths 2 cm and 1 cm, respectively. These values were selected based on studies in which these geometric features were quantified in Florida Harvester ant nests [42]. We verified that the pitch angle of the main shaft of the natural nest was in this general range of 20° and 70°. Specifically, the pitch angle of the main shaft of the natural nest was between 45°



 $\begin{tabular}{ll} Fig. 3 & 3D image of the post-processed casting used as input to the FEM model \\ \end{tabular}$

and 70° when measured locally along the depth, as shown in the left panel of Fig. 4. Helix diameters were reported to lie in the range of 4–6 cm with little variation over the depth of the shaft [42], which is why we used a unique median value of 5 cm for the helix diameter in our parametric study. The measure of the helix diameter of the main shaft in the natural nest was consistent with this choice. Each shaft geometry was created using the



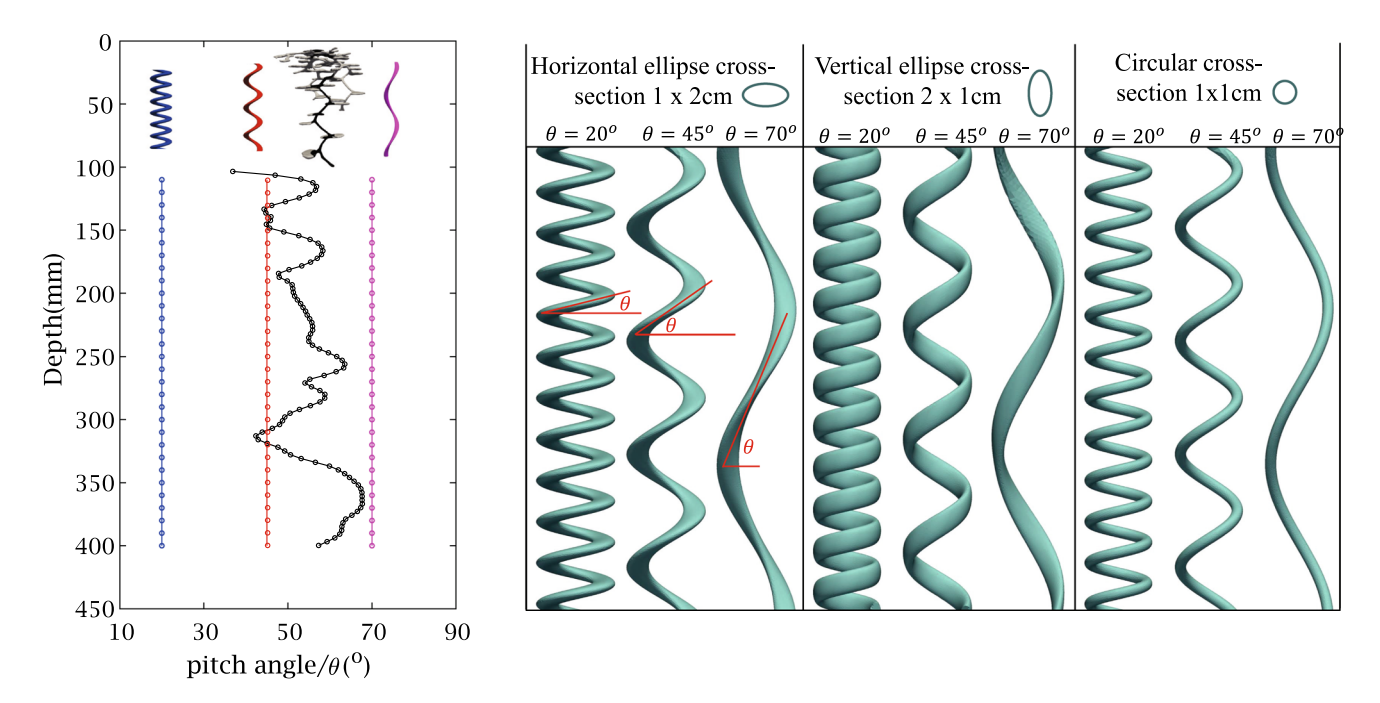


Fig. 4 Local pitch angle of the simplified field nest geometry shown in comparison with the pitch angle in the simplified shaft geometries (left); simplified ant shaft models used for benchmarking against portions of the actual scanned nest. θ denotes the pitch angle (right)

parametric equation of a helix, and the model generation was done through an automated routine that took the geometric variables such as pitch angle, cross-sectional shape, size, and orientation as inputs. The different geometries used are presented on the right panel of Fig. 4.

2.3 Finite Element models

Finite Element models of the simplified nest geometry and of the simplified shaft geometries presented in Sects. 2.2.2 and 2.2.3 were created by extruding the geometric shape of interest from a prismatic solid domain. The lateral faces of the domain were subjected to zero normal displacement and zero shear stress. The three translation degrees of freedom at the bottom face were fixed to zero, and the top surface was free of stress. Before extrusion, the solid domain (which represents the soil mass) was subjected to geostatic stresses, where the vertical stress field, which reflects the soil self-weight, is calculated as $\gamma_t \times z$ (z being the depth), and where the horizontal stress field, which represents the lateral earth pressure of the soil, is calculated as $K_0 \times \gamma_t \times z$, where K_0 is calculated by Jaky's equation [19]. Then static, implicit analysis was used to simulate the extrusion in one loading step, with a direct solver and a full Newton resolution technique.

2.3.1 Finite Element model of the simplified nest geometry

To create the Finite Element (FE) model of the soil surrounding the nest, the processed digital twin of the casting

was imported into the FE analysis software ABAQUS. The bounding box size of the processed casting was approximately $398 \times 341 \times 432$ mm³ $(L \times W \times H)$. The nest casting shape was extruded from a parallelepiped to create the simulation domain. We picked the smallest simulation domain size that ensured negligible displacement and stress gradient at the boundaries when performing the extrusion simulation under geostatic stresses, i.e., $600 \times 600 \times 625$ mm³ $(L \times W \times H)$. The geometry, boundary conditions, and geostatic loading are illustrated in Fig. 5.

The 3D domain was meshed using linear tetrahedral elements of type C3D4. The mesh was refined close to the ant nest walls. The Finite Element mesh, shown in Fig. 6, contained 559, 534 nodes and 3, 199, 559 elements.

2.3.2 Finite Element models for the simplified shaft geometries

The process to create simplified shaft models was similar to that used to create the simplified ant nest model. The simulation domain for each shaft was a cylinder of radius 125 mm and height 600 mm. The height of a shaft in that domain was 450 mm. The distance between the shaft walls and the outer domain boundaries was similar to that between the ant nest walls and the domain boundaries in the previous model, and we checked that the domain extent chosen for the simplified shafts was large enough to avoid boundary effects. We used linear tetrahedral elements (C3D4), and the mesh was refined close to the shafts in a



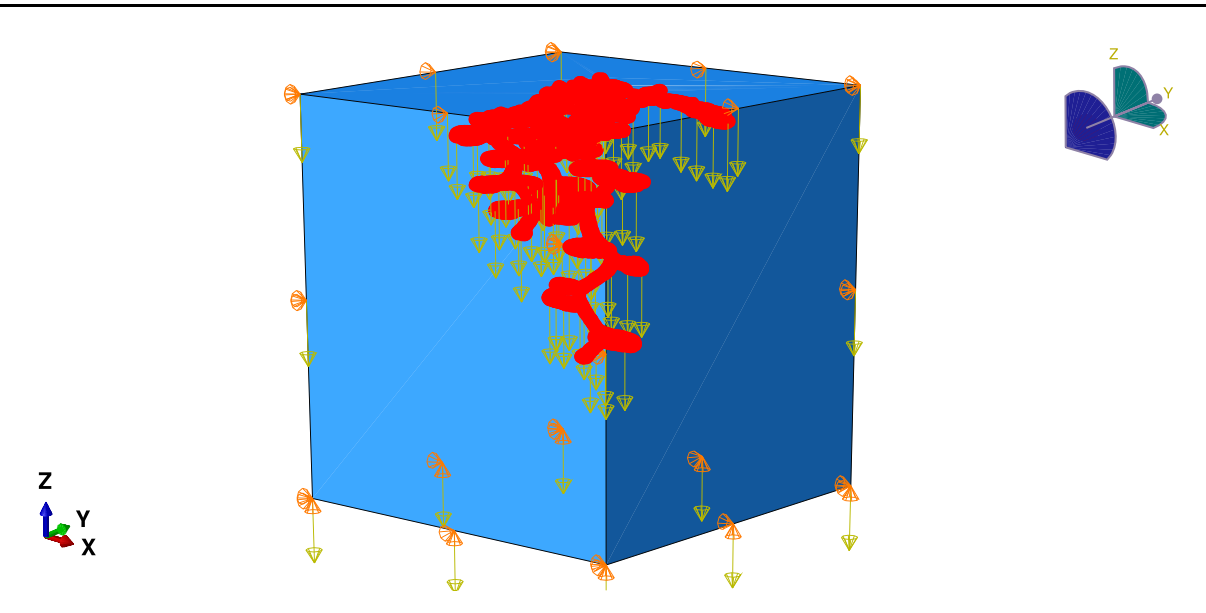


Fig. 5 Finite Element model of the simplified ant nest cast in situ, with loading and boundary conditions (soil domain shown in blue and nest walls in red). Domain size: $600 \times 600 \times 625 \text{ mm}^3 (L \times W \times H)$

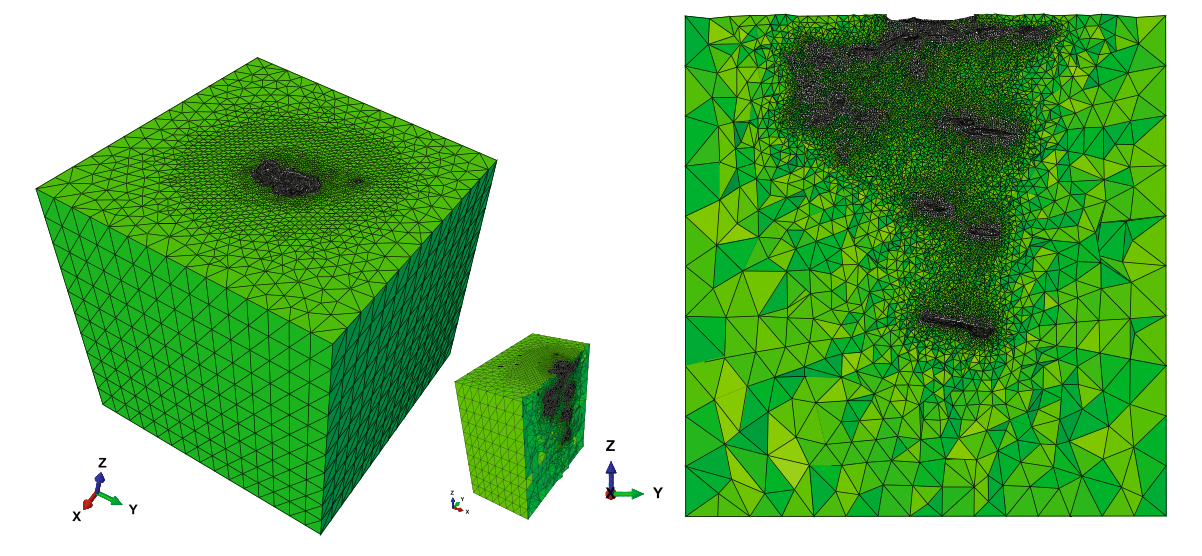


Fig. 6 Finite Element model mesh for the soil domain around the ant nest

manner similar to the one shown in model of the ant nest in Fig. 6.

2.4 FEM result post-processing

We enhanced open-source codes available in the literature [23] to convert ABAQUS output files from ".odb" to ".vtk" (visualization toolkit) format, which allowed us to use ParaView to create visualizations of the results of the three-dimensional FE simulations explained in Sect. 2.3. ParaView is a powerful tool for volume rendering which is useful to visualize the data in a solid 3D domain; extraction of slices and sub-volumes for visualization; extraction of numerical data at any coordinates within the 3D domain,

regardless of the position of the Finite Element nodes. Additionally, ParaView offers many filters, one of which allows calculation of new fields of data from the existing FEM output fields. Lastly, ParaView has a Python scripting interface that can be used to automate data extraction, which was crucial for analyzing the data around the shafts and chambers of the nest. We compared the stress and displacement fields around the longest helical shaft of the ant nest with those around the simplified shaft models. To do so, we took slices of the deformed mesh normal to the path of the helix. This required extracting the center-line of the helix (a process called skeletonization) so as to generate unit vectors along the helix path. The procedure to extract data is explained below for the model of the ant nest. The



method employed to post-process the Finite Element output data obtained from the simplified shaft simulations was similar.

2.4.1 Skeletonization and unit vector extraction

Skeletonization was done with an open-source L1-median algorithm [18], which fits an ellipse to a group of points intersected by a small plane surface that travels around the domain and then finds the centroid of that ellipse. These barycenters are then assembled together to form the centerline of the shape under study, and the skeleton is obtained. The L1-median algorithm was suitable for our purpose, since the cross-sections of the helical shafts were expected to be elliptical both in the processed digital images of the field cast and in the simplified shaft models. Figure 7 illustrates the principle of the skeletonization algorithm.

The skeleton of the main shaft was extracted for depths between 10 cm and 40 cm. The coordinates of the points on the center-line were used to generate unit vectors along the path of the helix at regular intervals. Figure 8 shows the skeleton of the main shaft of the ant nest (left panel), along with sample normal planes and the unit vectors normal to them (right panel).

2.4.2 Data extraction and filtering

Finite Element simulation output data were extracted along the planes normal to the skeleton. In ParaView, the field variables calculated at the nodes or Gauss points of the elements intersected by the normal planes were interpolated so as to generate maps of field variables on the normal planes (see the left panel of Fig. 9). Out of these field variable maps, we extracted the data points located at the walls of the nest structure from the knowledge of the coordinates of the points on the surface contour of the nest (see the second figure from the left panel in Fig. 9). The contour plots at the walls of chambers were filtered out in order to display contour plots of the field variables at the wall of the main shaft only (see the third figure from the left panel in Fig. 9). In order to display the results in a local coordinate system in which the horizontal axis always refers to the direction of the major axis of the shaft section being intersected, we fit an ellipse passing through all the points of the shaft wall, and we calculated the angular coordinate (α) of these points in reference to the centroid and major axis of the ellipse (see the right panel of Fig. 9). At each point on the ellipse, we extracted the values of the displacement and stress fields. We then calculated the stress invariants at each point.

3 Results and discussion

The results of the FE analysis show that, under the constitutive modeling assumptions made in this study, the domain is fully in elasticity and that there is no plasticity developed. The main results that we interpret below are the first stress invariant I_1 and the second invariant of the deviatoric stress tensor J_2 :

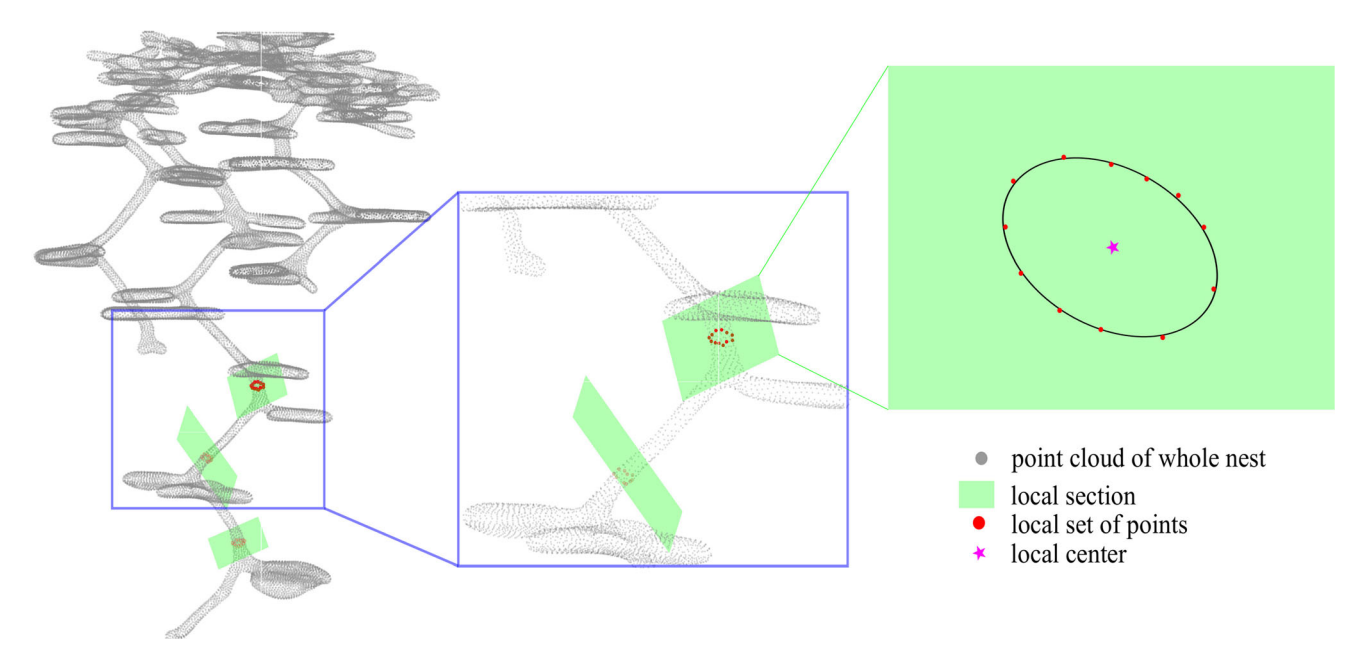


Fig. 7 Principle of the skeletonization process based on an L1-median algorithm that recenters a center-line by local ellipse fitting



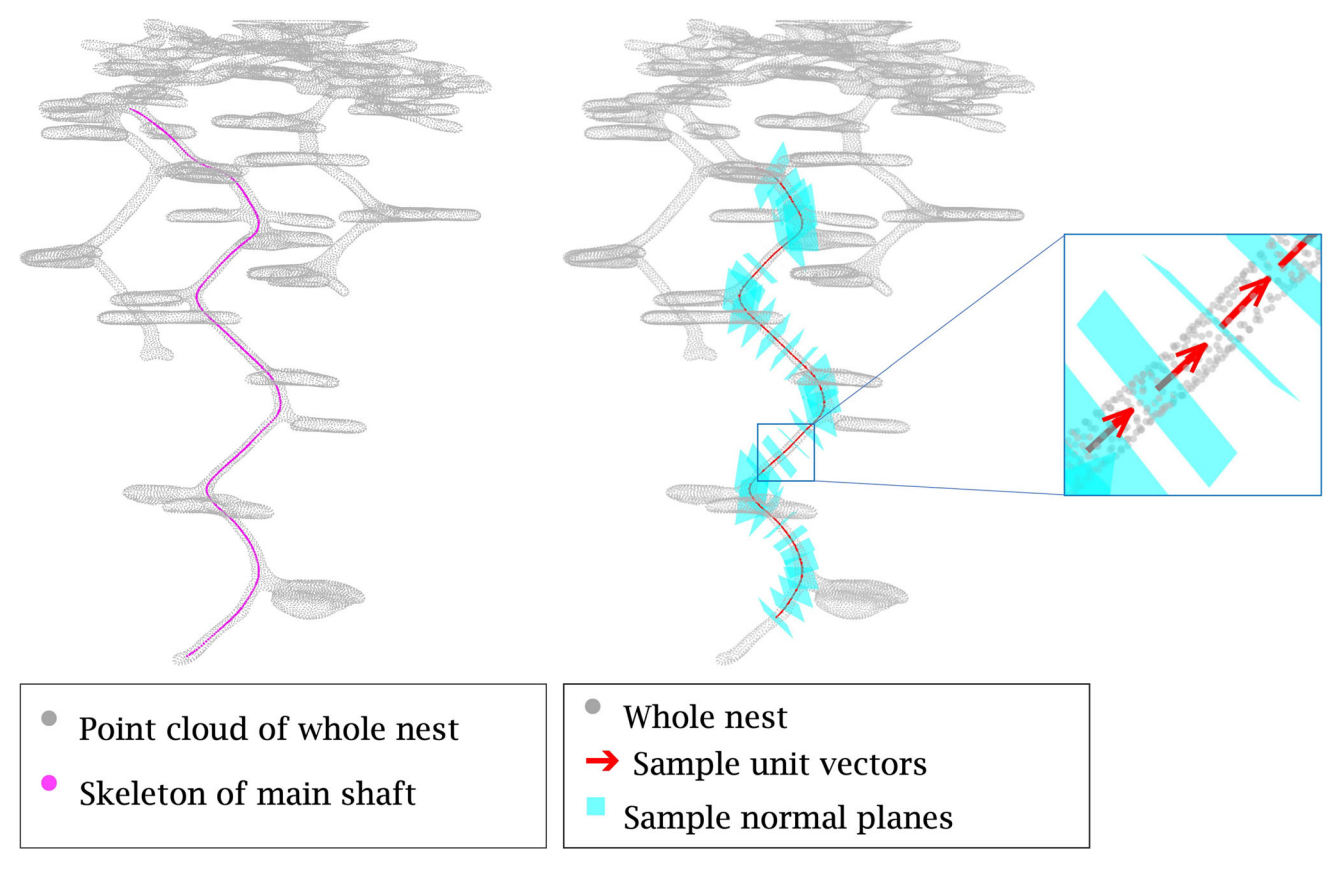


Fig. 8 Skeleton of the main shaft of the ant nest (left) and sample normal planes with the unit vectors orthogonal to them (right)

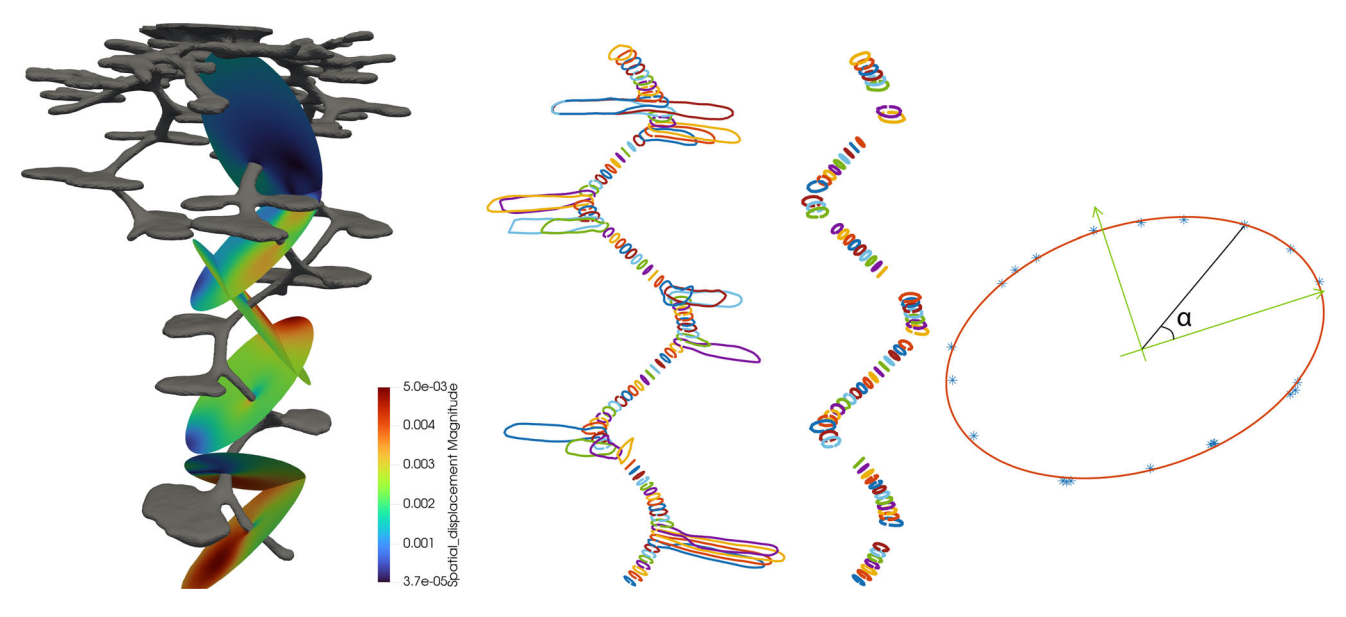


Fig. 9 Sample field data of spatial displacement shown around the main shaft (left); filtered coordinates at the nest walls and at the shaft walls only (middle two); sample ellipse fit for a local cross-section, and calculation of the angular coordinates α of the points of the ellipse in reference to the ellipse major axis (right)

$$I_{1} = \sigma_{xx} + \sigma_{yy} + \sigma_{zz}$$

$$J_{2} = \frac{(\sigma_{xx} - \sigma_{yy})^{2} + (\sigma_{yy} - \sigma_{zz})^{2} + (\sigma_{xx} - \sigma_{zz})^{2}}{6} + \sigma_{xy}^{2} + \sigma_{yz}^{2} + \sigma_{zx}^{2}$$
(3)



In the following, compression is counted positive (per the soil mechanics sign convention). I_1 is three times the mean stress. A negative or close-to-zero value of I_1 is indicative of a risk of tensile failure. J_2 reflects the effect of shear stress. A high value of J_2 points toward an increased risk of shear failure according to Mohr–Coulomb criterion and other failure criteria typical of frictional granular media.

3.1 Stress invariant extrema at shaft walls

The stress invariants are calculated at each point of the contour of the wall of the main shaft, following the procedure explained in Sect. 2.4.2. The extremum values of the invariants at the circumference of the shaft are then calculated for each shaft section that has been extracted, which allows plotting the extremum values of the invariants as a function of depth. Additionally, the invariants of stress at the same depths before nest extrusion (i.e., the invariants of the geostatic stress in the far field) are also calculated. We note the geostatic stress invariants I'_1 and J'_2 .

Figure 10 shows the variation of the maximum value of the first invariant normalized by the geostatic stress first invariant. A value close to one means that the maximum compression stress at the shaft wall is equal to the mean compression stress in geostatic conditions at the depth of observation. The results obtained for the main shaft of the ant nest model are compared with those obtained around simplified helical shafts with horizontal elliptical, vertical elliptical, and circular cross-sections, with pitch angles of 20° , 45° , and 70° . It is interesting to note that the

normalized maximum value of the first invariant is quasiindependent from depth for the idealized shafts, which means that the maximum value of I_1 follows a geostatic gradient at the wall of the helical shafts (despite the presence of that shaft). The idealized shafts with a horizontal elliptical cross-section exhibit higher maximum mean compression (about twice the mean compression under geostatic stress), while the idealized shafts with circular and vertical elliptical cross-sections have a maximum mean compression stress close to the geostatic mean compression stress. The normalized maximum value of I_1 at the wall of the main shaft of the ant nest varies non-monotonically with depth. The plot exhibits oscillations around the values of I_1/I_1' observed around idealized shafts. The local maxima of I_1/I'_1 around the natural shafts are found at the depths where the main shaft connects with a chamber, which indicates that the chambers redistribute geostatic stresses.

Figure 11 shows the non-normalized minimum value taken by the first invariant I_1 at the shaft wall, as a function of depth. None of the shafts under investigation exhibit a negative mean stress. Although this does not guarantee that none of the principal stresses are negative (i.e., a tension), this first control check indicates that none of the shafts are guaranteed to fail in tension. That being said, the value of the minimum mean stress (a third of I_1) is in the range of 0.5–3 kPa, which indicates that a small perturbation of the state of stress could lead to tension at the shaft wall, which itself could trigger failure. The normalized plots (not shown here for the sake of brevity) of the minimum value

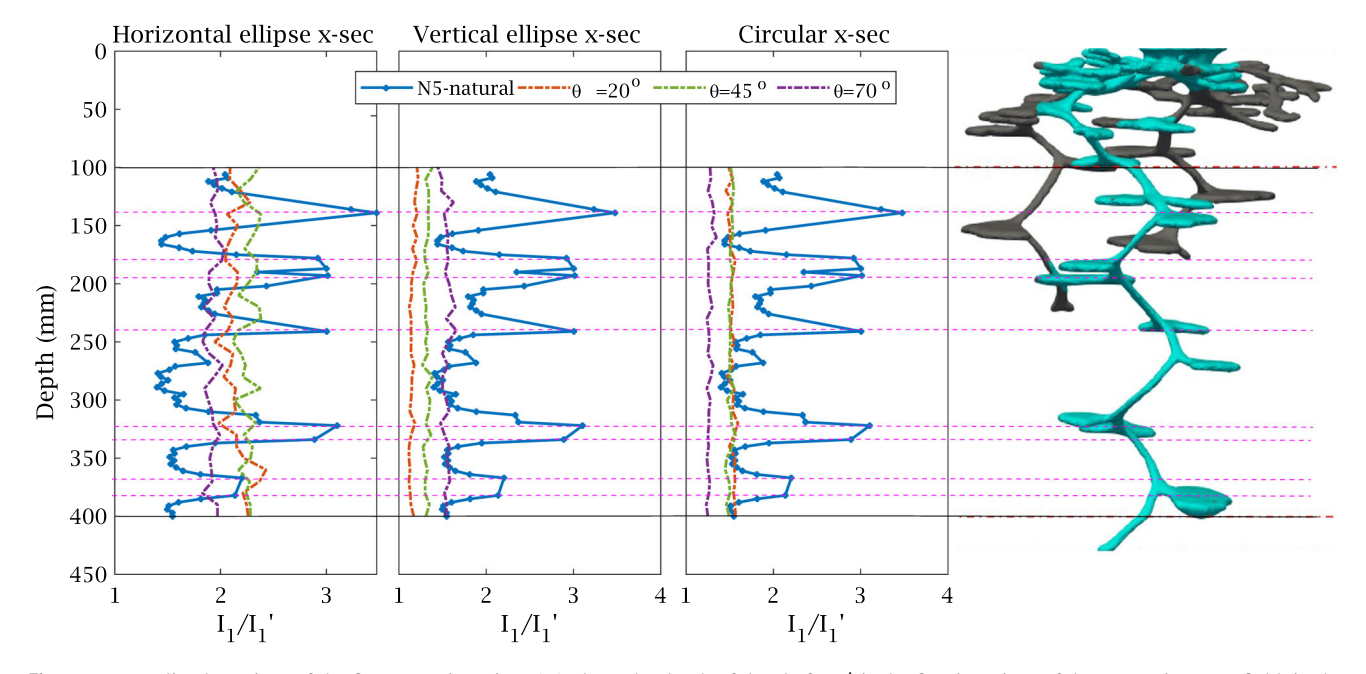


Fig. 10 Normalized maxima of the first stress invariant (I_1) along the depth of the shafts. I'_1 is the first invariant of the geostatic stress field, in the absence of shaft. The dashed lines mark the position of the chambers in the ant nest model



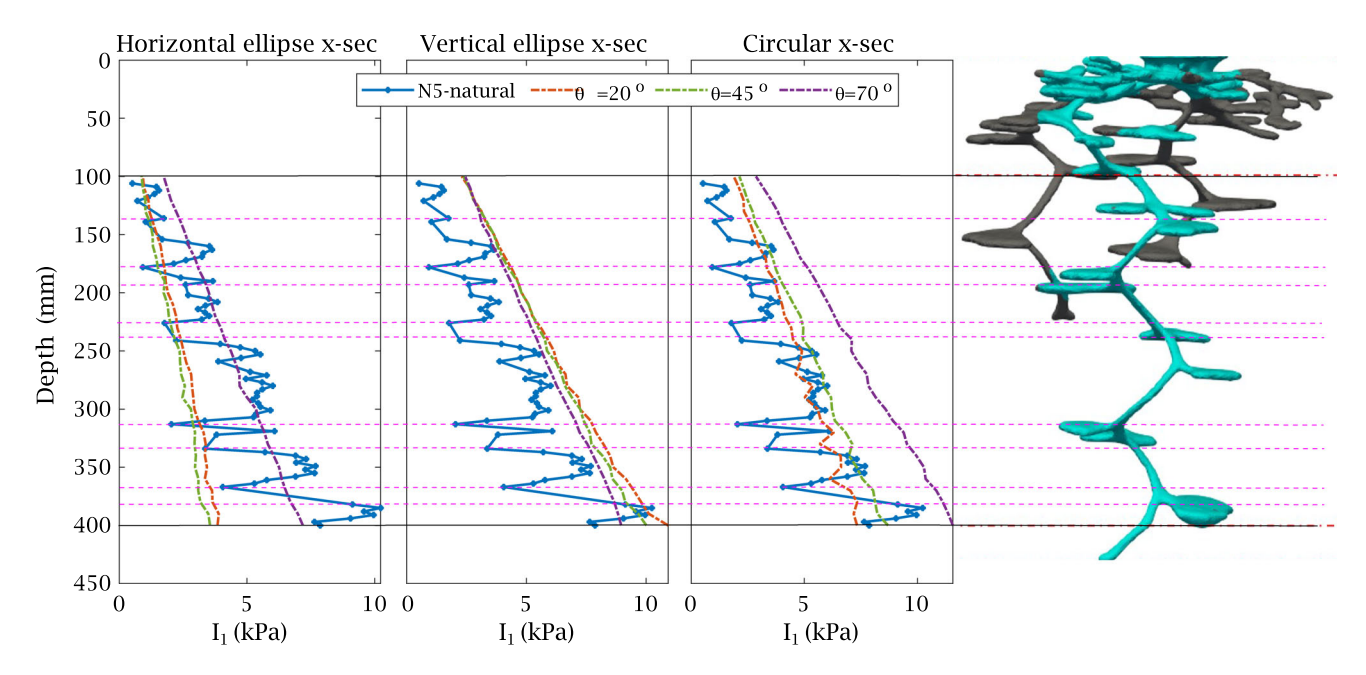


Fig. 11 Minima of the first stress invariant (I_1) along the depth of the shafts. The dashed lines mark the position of the chambers in the ant nest model

of I_1 at the wall of any of the shafts (including the main shaft of the ant nest) are lower than the first invariant of the geostatic stress field. At the wall of the idealized helical shafts, I_1 follows a geostatic (gravity-driven) gradient. The local minima of I_1 around the natural shafts are found at the depths where the main shaft connects with a chamber. This can be interpreted in the same way as for the maximum value of I_1 : The chambers redistribute geostatic stresses.

Figure 12 shows the maxima of the normalized second invariant of deviatoric stress at the shaft walls as a function of depth. The maximum second invariant at the walls of idealized shafts follows a geostatic gradient, which explains why the normalized second invariant J_2/J_2' is almost constant at all depths. Slight/larger oscillations (of amplitude of about 5% / 15% of the mean value) are noted for shafts of circular/horizontal elliptical cross-section. A

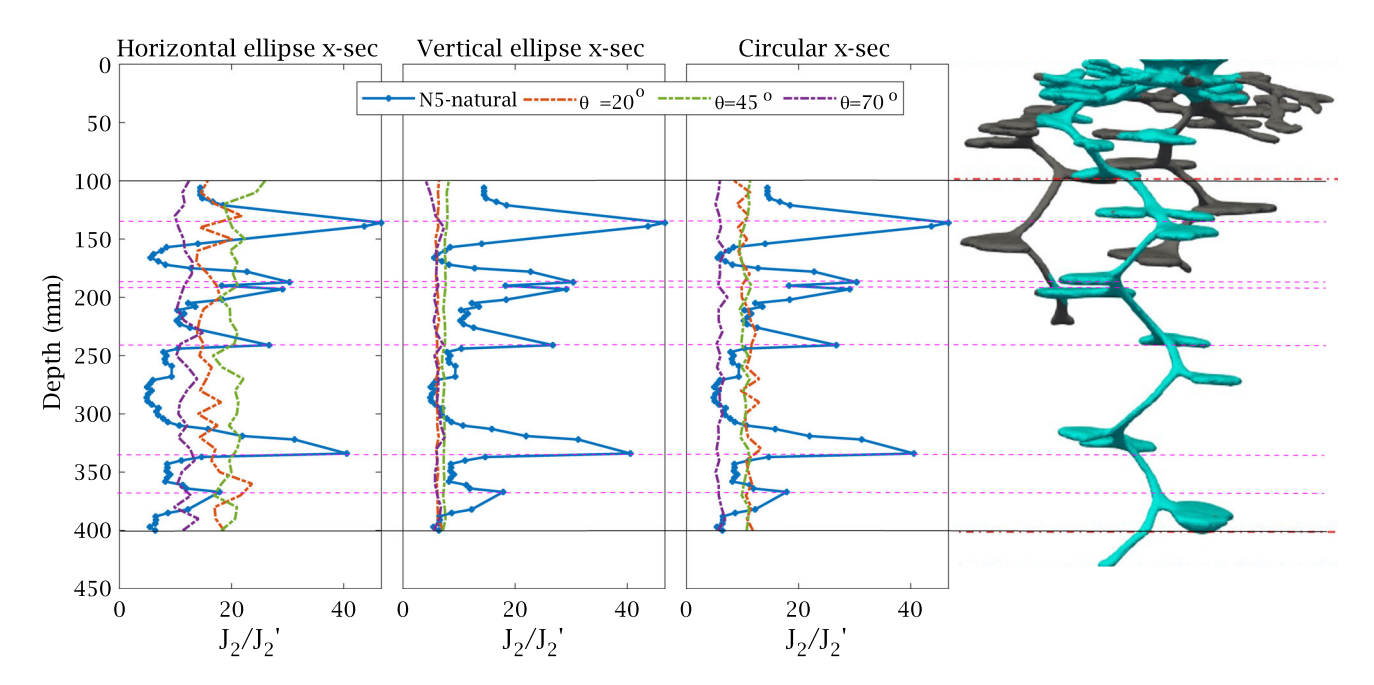


Fig. 12 Normalized maxima of the second invariant of the deviatoric stress (J_2) along the depth of the shafts. J'_2 is the second invariant of the deviatoric geostatic stress field, in the absence of shaft. The dashed lines mark the position of the chambers in the ant nest models



possible explanation for why the peak values of J_2/J_2' exhibit almost no oscillation around helical shafts of vertical elliptical cross-section is that, for that cross-section orientation relative to the far-field stress, the stress at the cavity wall is more evenly distributed, which means that the range of values taken by J_2 is narrower than for the other two types of cross-section (see the details in Sect. 3.2.2, Fig. 17, where we plot the distribution of the stress invariants around the cavity walls at different depths). Interestingly, all the maxima of J_2 around the shafts exceed the second invariant of the geostatic stress field. For idealized helical shafts of vertical elliptical cross-section, the maximum value of J_2 is about five times the value of J_2 that would exist under a geostatic stress field, while the maximum value of J_2 is 10 to 15 times (respectively, 10 to 20 times) larger than the value J_2 expected under geostatic stress conditions for a circular cross-section (respectively, a horizontal elliptical cross-section). The maximum value of J_2 at the wall of the main shaft of the ant nest model almost always exceeds the maximum value of J_2 at the wall of any idealized shaft at a given depth, except for the idealized shafts that have a horizontal elliptical cross-section. Additionally, the maxima of J_2/J_2' reached at the wall of the main shaft of the ant nest model exhibit peaks at depths just below the connections with chambers (one exception is the small peak observed at 380 mm depth). This reinforces once again the role of chambers in the redistribution of geostatic stresses.

The maximum value taken by the yield function f at any given depth is plotted in Fig. 13 for the simplified nest geometry and for the idealized shaft geometries. We recall

that the Mohr-Coulomb plasticity criterion in terms of stress invariants as:

$$f = \sqrt{J_2} - \frac{m(\theta_l, \phi) \sin \phi}{3} I_1 - m(\theta_l, \phi) c \cos \phi \tag{4}$$

where

$$m(\theta_l, \phi) = \frac{\sqrt{3}}{\sqrt{3}\cos\theta_l + \sin\theta_l \sin\phi}, \quad \sin 3\theta_l = \frac{3\sqrt{3}J_3}{2J_2^{3/2}},$$
$$J_3 = \det\left(\sigma - \frac{I_1}{3}\delta\right)$$

The closer f is to zero, the closer the stress state is to a plastic state. Results indicate that shafts with a pitch angle of 70° are the furthest from plasticity. The analytical solutions presented in the next section show that stress states in biaxial conditions are generally closer to plasticity than in isotropic conditions. The low value of f at a pitch angle of 70° can be attributed to the low anisotropy of the stress state. Shafts with vertical elliptical or circular crosssections present similar yield function profiles for pitch angles of 20° and 45°. For shafts with a horizontal elliptical cross-section, a pitch angle of 20° provides a state of stress that is generally further to plasticity than a pitch angle of 45°. This is counter-intuitive because the shafts of a smaller pitch angle are subjected to more of a biaxial stress state, which is expected to increase the risk of plasticity. This can be understood as the result of interactions between coils, which are closer to one another when the pitch angle is lower.

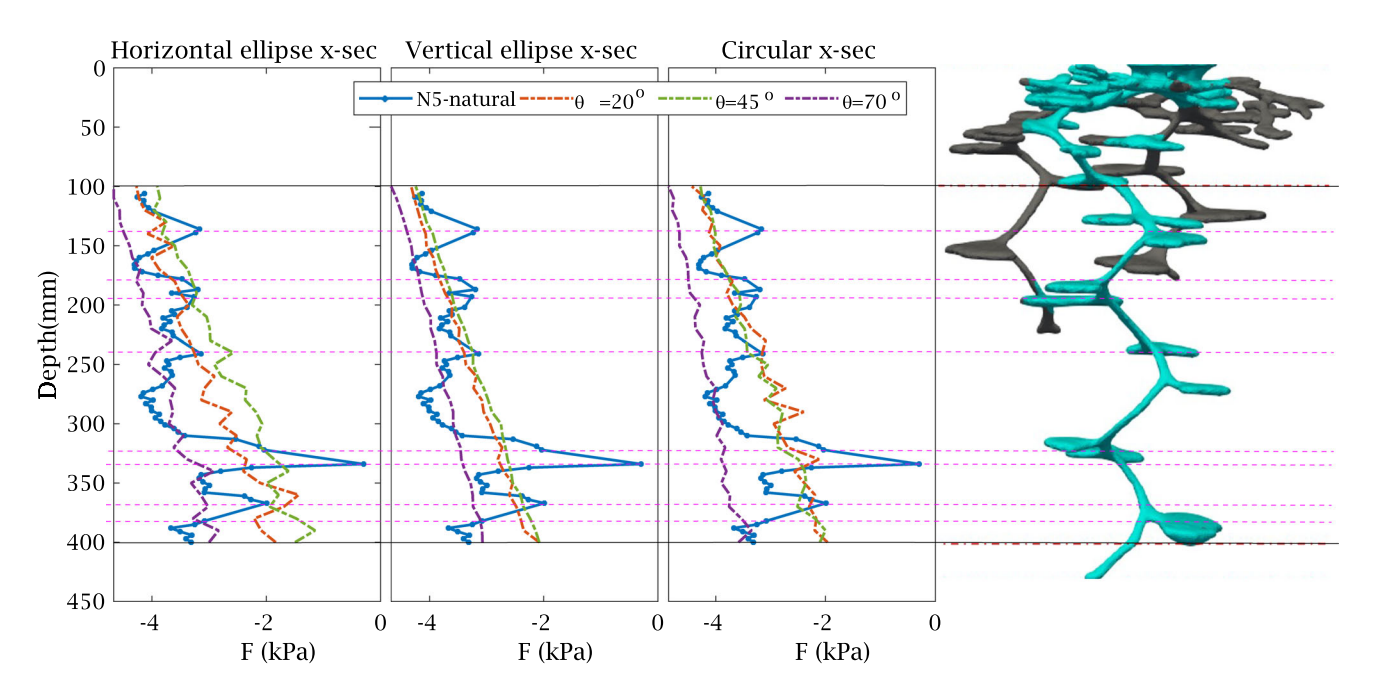


Fig. 13 Maximum value of the yield function at any given depth. The dashed lines mark the position of the chambers in the natural nest



3.2 I_1 and J_2 distributions around the shafts

3.2.1 Baseline analytical solution

Equations 5–7 provide the analytical expression of the stress field in an elastic medium around an elliptical cavity in plane strain [4], with the geometric parameters shown in Fig. 14. Since it was found that the soil never enters the plastic regime in our simulations, this analytical solution is sufficient to assess the stress distributions around the shafts in reference to those that would be obtained around a straight shaft under biaxial stress conditions (horizontal shaft) or isotropic stress conditions (vertical shaft embedded in a soil mass under isotropic horizontal stresses). The comparison of the analytical and simulated stress distributions allows isolating the effect of the helical geometry of the shaft on the mechanical state of the soil mass around the shaft.

For an ellipse that has its long axis oriented at an angle β compared to the direction of the horizontal and for a material element that is at coordinate (x_1, z_1) in reference to the shown coordinate system with the origin at the ellipse centroid and oriented at β from the horizontal, the stress components are given below. Note that the local coordinate system (l, m) corresponds to the perpendicular (l) and tangent (m) orientations in reference to the cavity wall.

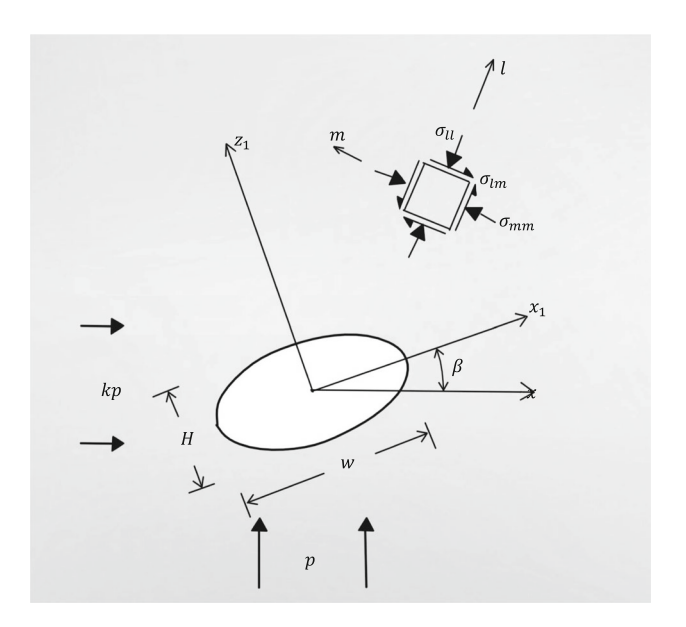


Fig. 14 Geometry of the problem in the analytical model of stress distribution around an elliptical cavity in plane strain

$$\sigma_{ll} = \frac{p(e_0 - e)}{J^2} \left[(1 + k(e^2 - 1) \frac{C}{2e_0} + (1 - k) \right]$$

$$\left[\left(\frac{J}{2} (e + e_0) + Ce \right) \right]$$

$$\cos 2(\psi + \beta) - C \cos 2\beta$$
(5)

$$\sigma_{mm} = \frac{p}{J} [(1+k)(e^2 - 1) + 2(1-k)$$

$$e_0(e\cos 2(\psi + \beta) - \cos 2\beta)] - \sigma_{ll}$$
(6)

$$\sigma_{lm} = \frac{p(e_o - e)}{J^2} \left[(1 + k) \frac{Ce}{e_0} \sin 2\psi + (1 - k) \right]$$

$$\left(e(e_0 + e) \sin 2\beta + e \sin 2(\psi - \beta) - \left(\frac{J}{2} (e_0 + e) + e^2 e_0 \right) \right]$$

$$\sin 2(\psi + \beta)$$

$$(7)$$

where:

$$e_0 = \frac{W + H}{W - H}$$

$$b = \frac{4(x_1^2 + z_1^2)}{W^2 - H^2}$$

$$d = \frac{8(x_1^2 - z_1^2)}{W^2 - H^2} - 1$$

$$C = 1 - e(e_0)$$

Figure 15 shows the distributions of the first and second stress invariants expected in elasticity at the wall of horizontal elliptical cavities ($\beta = 0$), circular cavities, and vertical elliptical cavities ($\beta = 90^{\circ}$) that have the same dimensions as the cross-sections of the idealized shafts (circular sections of diameter 1 cm or elliptical cross-sections with a major axis 2 cm long and a minor axis 1 cm long). Here, I_1 and J_2 are normalized by the invariants of the initial geostatic stress (stress before the extrusion of the shaft from the solid domain meshed in the Finite Element analysis). Since the stresses depend linearly on the vertical far-field stress p, the normalization has the advantage of yielding variables that do not depend on the far-field stress conditions used in the analysis, which removes the need to vary p in our parametric studies, that is to say, I_1/I_1' and J_2/J_2' do not depend on depth and can be represented by only studying different shaft cross-section geometries and different values of the parameter k (which is equal to the coefficient of earth pressure at rest in biaxial stress conditions and equal to 1 in isotropic stress conditions).

3.2.2 Stress invariants around idealized shafts

Stress around a vertical shaft is close to isotropic, and stress around a horizontal shaft is close to biaxial, so it is expected that the idealized shafts with a pitch angle of 70°



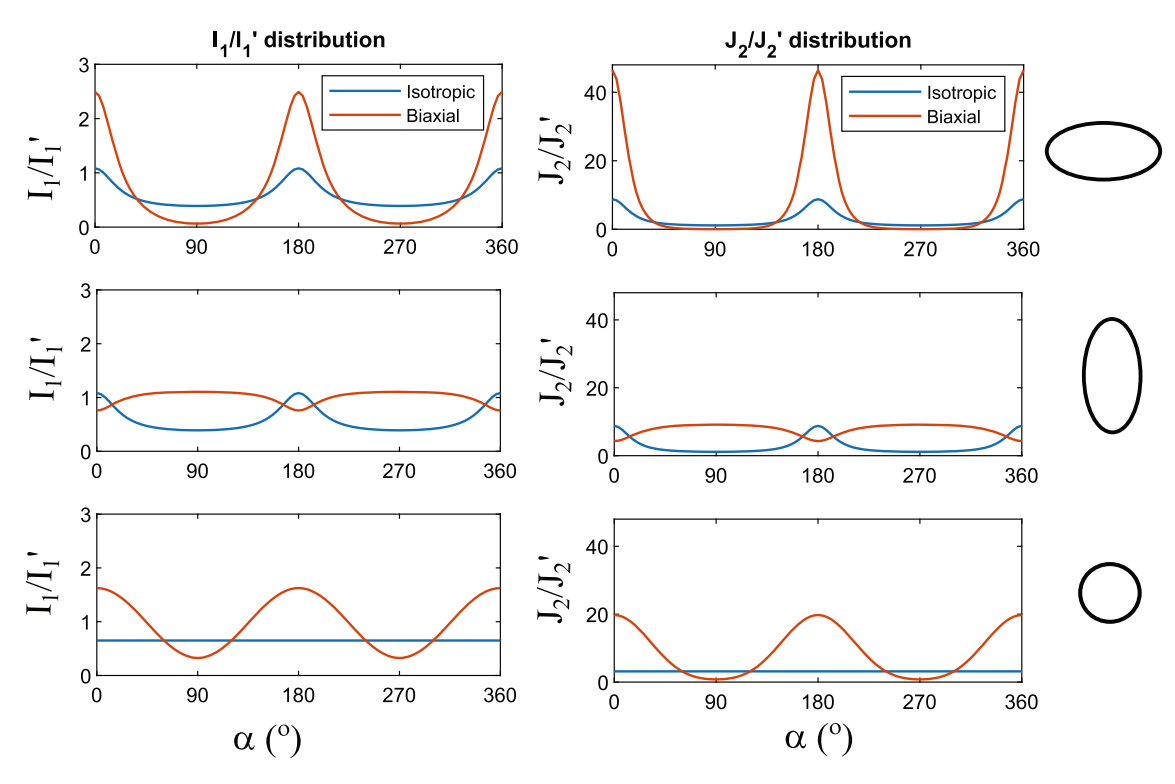


Fig. 15 Distributions of the normalized stress invariants at the wall of elliptical and circular cavities, calculated from the analytical solution. I'_1 is the first invariant of the geostatic stress field, and J'_2 is the second invariant of the deviatoric geostatic stress field (both I'_1 and J'_2 are calculated in the absence of shaft)

will exhibit a stress distribution close to that around a cavity subjected to isotropic stress in the far field, while the ones with a pitch angle of 20° will have a stress distribution close to that around a cavity subjected to a biaxial stress in the far field. The stress distributions at the contour of the idealized shafts are compared to those around elliptical cavities in plane strain in Fig. 16 (in terms of the first invariant) and in Fig. 17 (in terms of the second invariant).

The curve that represents the variations of I_1 with the angular coordinate α along the contour of shafts with a horizontal elliptical cross-section lies between the curves obtained analytically for a straight shaft under biaxial and isotropic stress conditions. For helical shafts of circular cross-section, the variations of I_1 are similar to those obtained analytically under biaxial stress conditions, but the curve is translated by about 45° and reaches higher minima than with the analytical solution under biaxial stress. If the cross-section is a vertical ellipse, the variation of I_1 with α is similar for the idealized shaft models and the analytical solution (around one). We expected instead that the idealized shafts would follow a stress distribution similar to the one obtained analytically in isotropic conditions for a pitch angle of 70° and similar to the one obtained analytically in biaxial conditions for a pitch angle of 20° . This is because the coils of the helical shafts interact with one another. According to the analytical

solution for a horizontally oriented elliptical cavity in a biaxial far-field stress state, there is a risk of tension failure at the crown and at the foot of the cavity as can be indicated by the nearly 0 or negative I_1 values. At the crosssection of a helical shaft with a horizontally oriented ellipse at a 20° pitch, which is close to a horizontal elliptical cavity under biaxial stress, tension is avoided due to the interaction between the different segments of the helix. Such interaction is also visible in the plots obtained for circular sections at a 20° pitch. The redistribution of stress at the wall of helical shafts with a vertical elliptical crosssection is more complex to interpret, and the interaction is less significant. This is likely because the distance between the coils is too small to allow the type of interactions seen in the other two cross-section shapes, and the orientation of the cross-section relative to the geostatic stresses in the far field does not create influence zones that allow the interaction that is observed in the case of horizontal elliptical cross-sections. At a 70° pitch angle, the average compression stress at the cavity wall is larger than under isotropic stress for all section shapes, which points to favorable interactions between the coils. The variations of I_1 around the sections of the shafts oriented at a pitch angle of 45° follow the same trends as for the other pitch angles, with intermediate magnitude values.



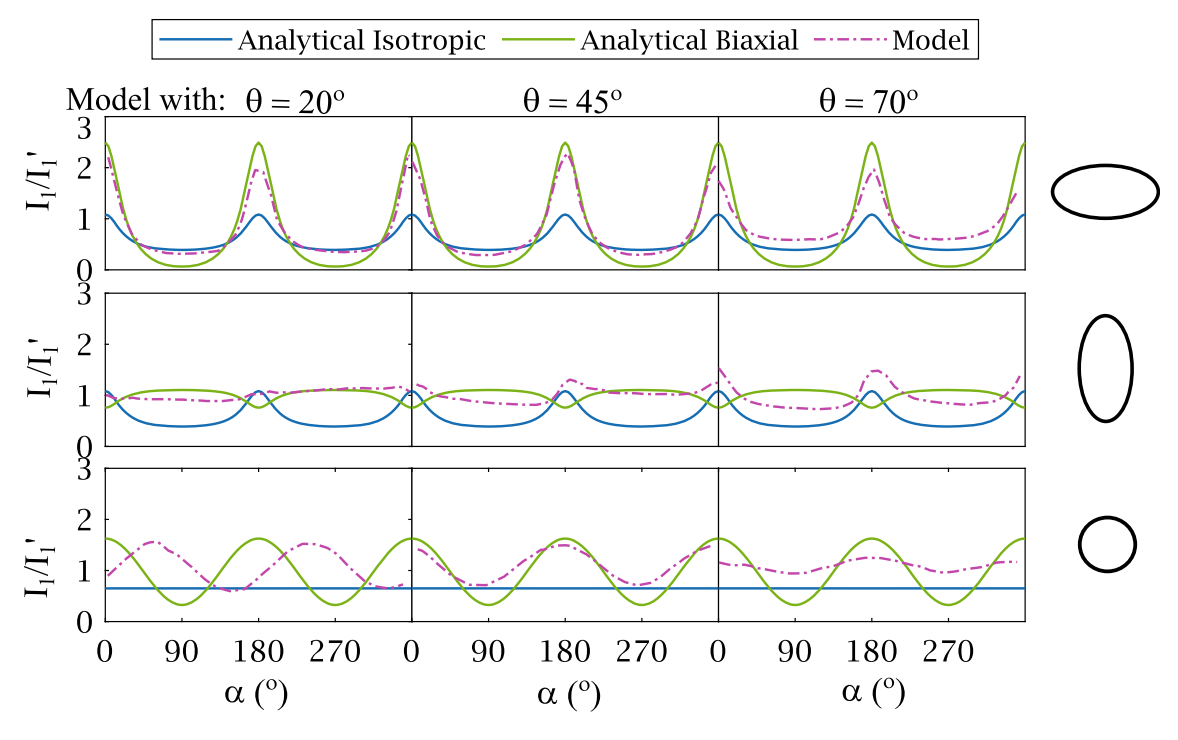


Fig. 16 Normalized I_1 distribution around the cavity wall: comparison between analytical solution and idealized shaft models for several pitch angles (θ) . I'_1 is the first invariant of the geostatic stress field, in the absence of shaft

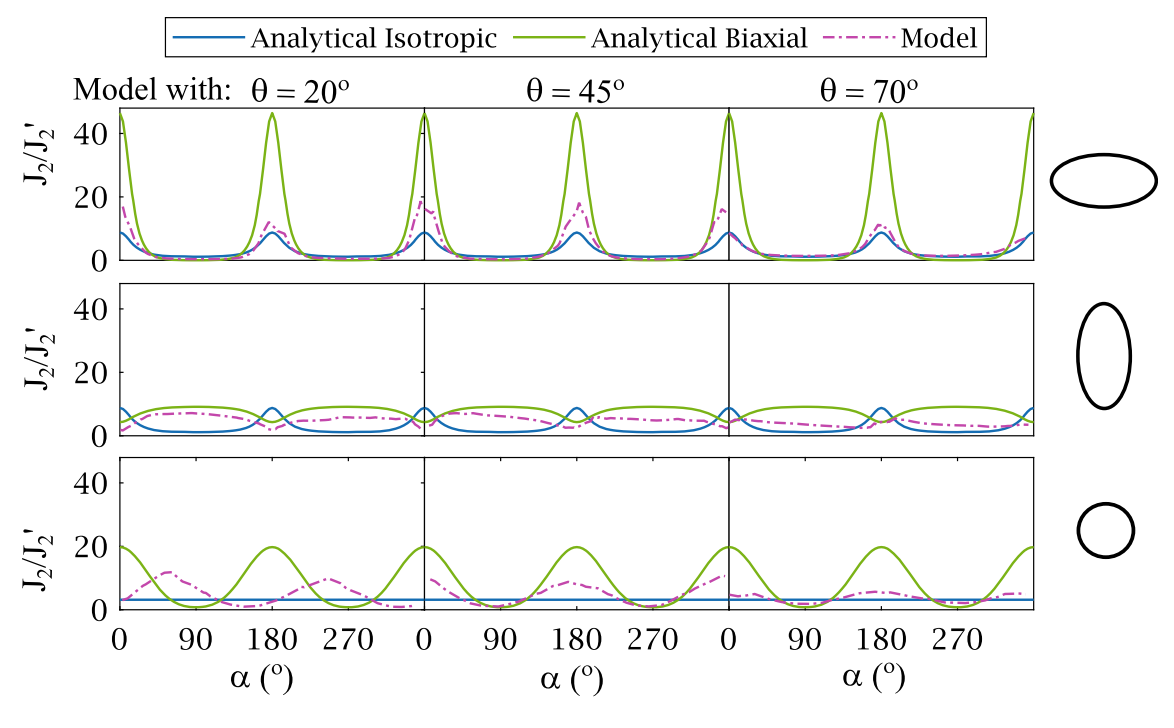


Fig. 17 Normalized J_2 distribution around the cavity wall: comparison between analytical solution and idealized shaft models for several pitch angles (θ) . J'_2 is the second invariant of the deviatoric geostatic stress field, in the absence of shaft

The variations of J_2 with the inclination angle α along the contour of the idealized shafts follow the analytical solution obtained for biaxial stress conditions if the shaft cross-section is a horizontal ellipse, but the peak values of

the J_2 are 3–4 times lower than in the analytical solution. If the cross-section is circular, the variations of J_2 are also similar to those obtained analytically under biaxial stress conditions with lower magnitudes, but the curve is



translated by about 45°. If the cross-section is a vertical ellipse, the curve showing the variations of J_2 with α lies between the ones obtained analytically for biaxial and isotropic stress conditions. Overall, what is striking is that compared to the known analytical solutions, for a given cross-section shape, J_2 is more evenly distributed around the wall of helical shafts. This implies that there is a decreased risk of shear failure. We hypothesize that this is due to the interaction between the coils of the helix. The redistribution of the variations of J_2 compared to the stress distributions in biaxial stress is more prominent for horizontal elliptical cross-sections, which could be due to arching effects made possible due the increased distance between the coils compared to the other cross-section shapes, or to the shielding effects induced by the zone of influence of elliptical cavities, which spreads over a larger vertical distance when the elliptical cavity is horizontal than when it is vertical [4]. It is interesting to note that interactions between coils contribute to the reduction of the magnitude of J_2 but not I_1 around circular shafts. Another noteworthy observation is that the values of J_2/J_2' are bounded by the values obtained analytically under isotropic and biaxial stress conditions in plane strain.

3.2.3 Stress invariants around the ant nest model

Figures 18 and 19 show the variations of the normalized first and second invariants at different depths around the

main shaft of the ant nest model and around the idealized helical shafts. Note that the curves obtained for the ant nest model are the same in each row, in which the cross-section of the idealized shafts is changed, but not that of the main shaft of the ant nest, which is taken as is from the digital images. A first glance at the figure indicates that, in general, the distributions of both I_1 and J_2 are close to those obtained around a helical shaft of horizontal cross-section with a pitch angle of 45° at shallow depth (190 mm), and they are close to those obtained around a helical shaft of circular cross-section at larger depth (400 mm). This agrees with the observations made in the field, where it was noted that the higher traffic close to the free surface causes cross-sections to be wider and more elliptical at shallow depth. The stress invariant distributions around helical shafts with vertical elliptical cross-sections do not reproduce the variations of stress invariants around the ant nests. The primary reason for this could be that ants are unlikely to excavate tunnels with that section shape, which does not allow more traffic and yet requires more mass removal.

Interestingly, the distribution of I_1 shows that in the ant nest model, the risk of tension failure is avoided by a higher degree as compared to the simplified models. At intermediate and larger depths (300 mm and 400 mm), it is worth noticing that the second invariant is more evenly distributed around the main shaft of the ant nest than around the idealized helical shafts, which implies that the risk of shear failure is lower than around helixes. These two

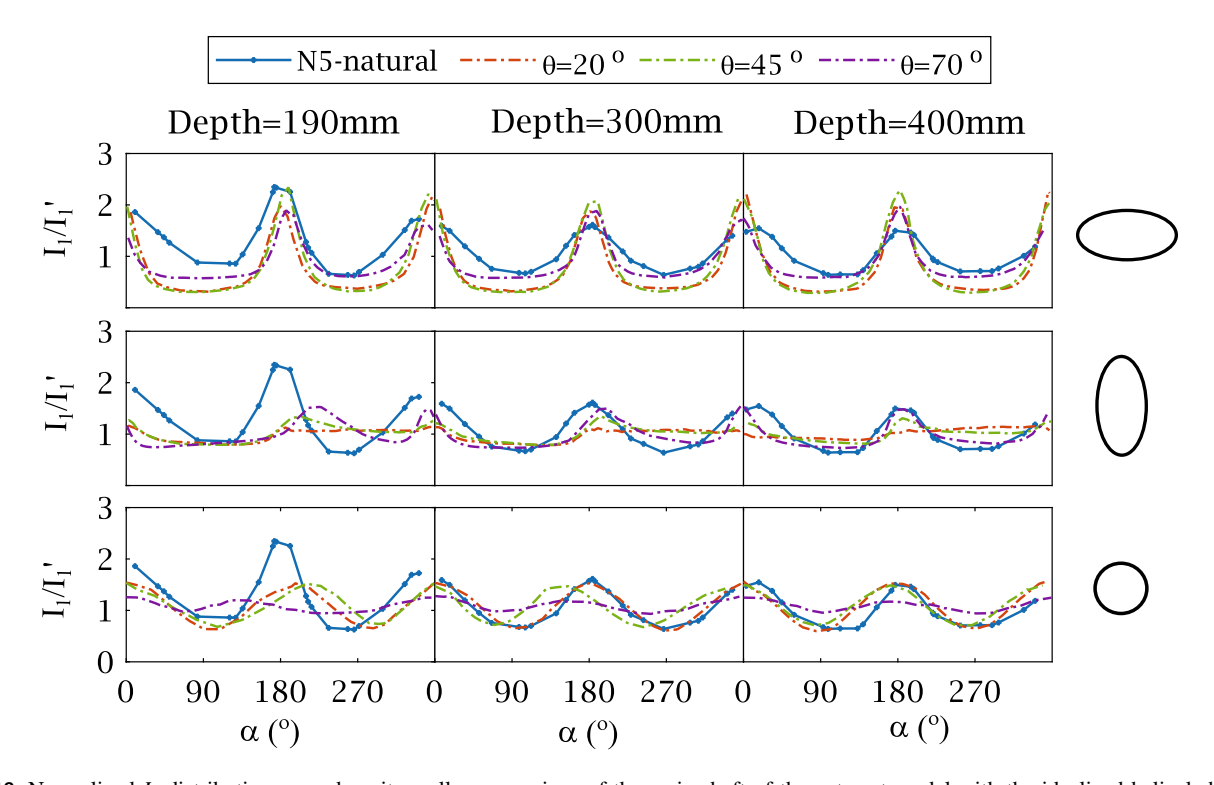


Fig. 18 Normalized I_1 distribution around cavity walls: comparison of the main shaft of the ant nest model with the idealized helical shafts



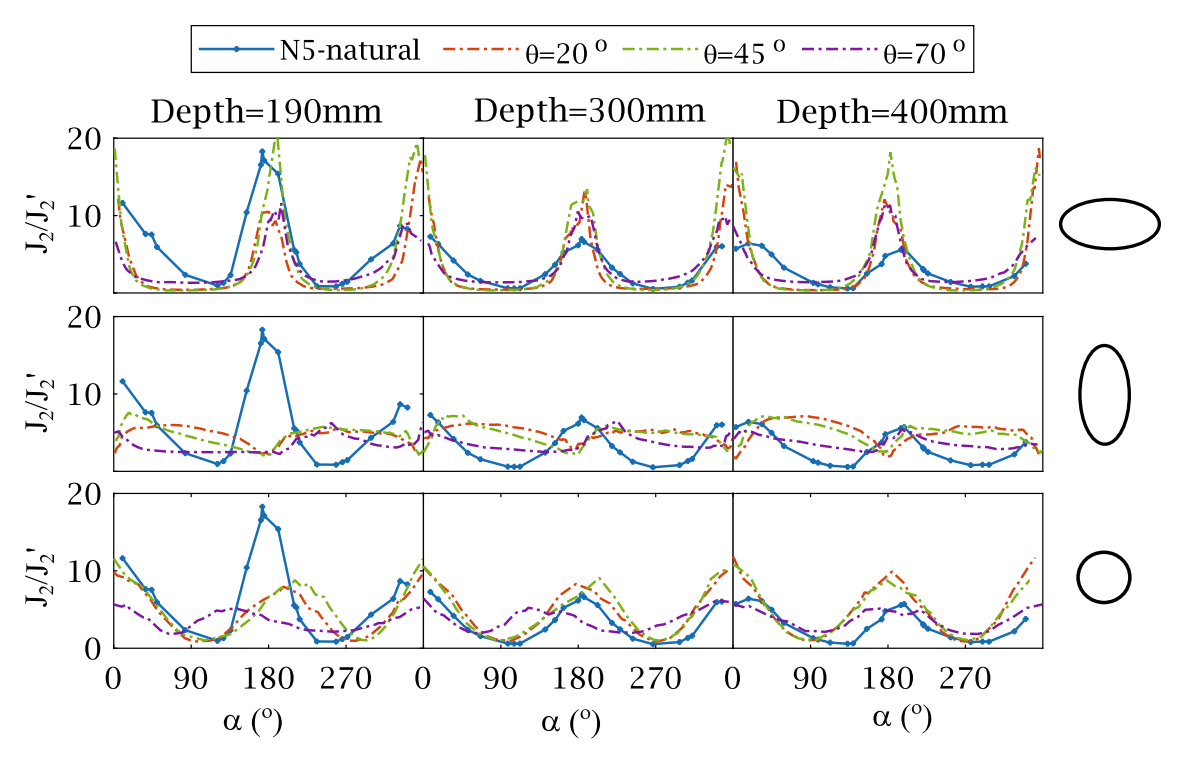


Fig. 19 Normalized J₂ distribution around cavity walls: comparison of the main shaft of the ant nest model with the idealized helical shafts

observations can be explained either by the irregular crosssectional size, shape, and orientation of the shaft in the ant nest or by the interactions with the remainder of the nest (other minor shafts and extending chambers) in the ant nest.

3.3 Comments on the helical shape of the main shaft

Beyond the reduced risk of tension or shear failure at cavity walls and increased stability of the underground structure, it is interesting to note some other benefits of the helical shaft shape. A simple intuitive analysis of excavation efficiency can be done between a helical vertical shaft and a nearly straight vertical shaft. During the excavation process, ants carry the sand particles out of the nest. In doing so, they walk uphill by providing mechanical work against their weight, as shown in the sketch in Fig. 20 (right panel). The work that needs to be produced to move upward by a distance δ along the slope $(mg \sin \theta \times \delta)$ increases as θ increases, i.e., as the slope becomes steeper. The path formed by a straight shaft between two points A and B has a steeper slope than any helical path between A and B, as shown Fig. 20 (left panel). Excavating a helical shaft requires removing more mass than excavating a nearly straight shaft, which may require more energy. But, at the same excavation rate, the power needed to excavate a section δ of the shaft at any given time, $mg \sin \theta \times \delta$,

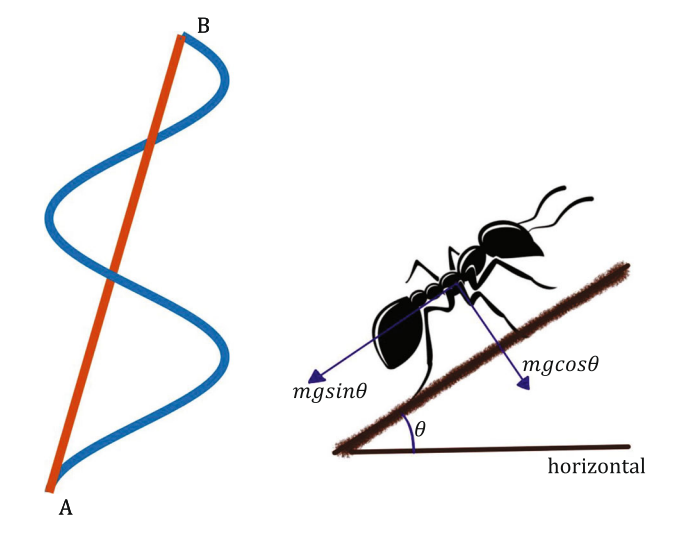


Fig. 20 Alternative paths from A to B with a straight shaft shown in orange and a helical shaft shown in blue (left). Force components involved in the work that ants have to do when carrying particles out of the ground

decreases as θ decreases. As a result, the helical shaft is a beneficial design when excavation power is limited. Other benefits to the helical shape may be found in the function that they serve for the ant communities as well, but this kind of multi-functional optimization problem is beyond the scope of the present study.



4 Conclusion

We modeled the complex underground structures of ant nests by in situ casting, 3D scanning, image post-processing, and Finite Element simulation and created simplified geometries that mimic the most unique geometric feature of the nest, i.e., helical shafts. The results obtained by calculating the stress distributions around a model of ant nest were compared to those obtained with idealized helical shaft models. The following general main observations were made:

- Coils of helical structures made of circular crosssections and horizontally oriented elliptical cross-sections interact in a way that reduces the risk of tension failure and distributes the shear stress more evenly;
- The pitch angle plays an important role in the intensity of these interactions;
- The maximum and minimum stress invariants I₁ and J₂ along cross-sections taken at different depths are significantly affected by the proximity of cross-sections to a chamber;
- The stress distributions around the cross-section of the main shaft in an ant nest resemble those around horizontal elliptical cavities at shallow depth and those of circular cavities at greater depth. This is in agreement with observations made in the field, where it was noted that the cross-section of the main shaft was wider close to the free surface, possibly to allow more traffic;
- In addition to promoting mechanical stability, helical shafts present the advantage of requiring lower excavation power than straight shafts.

An important consideration in bio-inspired geotechnics is the realization that biological solutions are multi-faceted. Organisms adapt to create a particular solution under a set of constraints. For example, ants, in constructing their nests, would be interested in optimizing their construction in a way that minimizes their excavation efforts, maximizes the nest stability and capacity, allows them to obtain food and store it easily, has good ventilation, and much more. It is important to disentangle and understand these aspects and then select strategies toward improving humandesigned systems. In this study, we presented a set of results that were created to understand the mechanical stability of ant nests. We learned that there is an advantage to creating helical shafts and we can argue that studies on such helical shafts could be useful to develop new technologies toward large-scale underground facilities with multiple levels that would be accessed through helical shafts. At a smaller scale, this knowledge can be used for deploying self-burrowing investigation robots that would construct helical structures, which have advantageous stability properties, thus enabling the robot to take the same path backward to be recovered. In order to evaluate these potential applications, it is necessary to study excavation energy efficiency and feasibility in further research.

Acknowledgments This material is based upon work primarily supported by the National Science Foundation under Grant No. 1935548 and partially through the NSF funded ERC on Bio-mediated and Bioinspired Geotechnics (CBBG) through PTE Federal Award No. EEC-1449501. Any opinions, findings, and conclusions or recommendations expressed in this material are those of the author(s) and do not necessarily reflect the views of the National Science Foundation. Funding was also provided by UKRI NERC grant NE/T010983/1.

Author contributions MB was involved in conceptualization, methodology, software, validation, formal analysis, investigation, data curation, writing—original draft, writing—review and editing, and visualization. KY was involved in methodology, investigation, resources, and writing—review and editing. EN and DZ participated in data curation, writing—review and editing, and visualization. DF participated in conceptualization, methodology, investigation, resources, data curation, writing—review and editing, supervision, project administration, and funding acquisition. CA was involved in conceptualization, methodology, formal analysis, resources, writing—original draft, writing—review and editing, supervision, project administration, and funding acquisition.

References

- Aleali SA, Bandini P, Newtson CM (2020) Multifaceted bioinspiration for improving the shaft resistance of deep foundations. J Bionic Eng 17(5):1059–1074. https://doi.org/10.1007/s42235-020-0076-6
- Anselmucci F, Andò E, Viggiani G et al (2021) Imaging local soil kinematics during the first days of maize root growth in sand. Sci Rep 11(1):1–13
- Anselmucci F, Andó E, Viggiani G et al (2021) Use of x-ray tomography to investigate soil deformation around growing roots. Géotech Lett 11(1):96–102
- Brady B, Brown E (2004), Rock mechanics for underground mining Third, vol 1. Kluwer Academic Publishers, arXiv:1011. 1669v3
- Burrall M, Dejong JT, Martinez A et al (2021) Vertical pullout tests of orchard trees for bio-inspired engineering of anchorage and foundation systems. Bioinspiration Biomim. https://doi.org/ 10.1088/1748-3190/abb414
- Coutts MP (1983) Root architecture and tree stability, Springer Netherlands, Dordrecht, pp 171–188. https://doi.org/10.1007/ 978-94-009-6833-2_18
- Das BM (2010) Principles of geotechnical engineering, 7th edn. CENGAGE learning
- 8. Del Dottore E, Mondini A, Sadeghi A, et al (2018) An efficient soil penetration strategy for explorative robots inspired by plant root circumnutation movements. Bioinspiration Biomim
- Dorgan KM (2015) The biomechanics of burrowing and boring.
 J Exp Biol 218(2):176–183. https://doi.org/10.1242/jeb.086983
- Dorgan KM (2018) Kinematics of burrowing by peristalsis in granular sands. J Exp Biol. https://doi.org/10.1242/jeb.167759
- Espinoza DN, Santamarina JC (2010) Ant tunneling-A granular media perspective. Granul Matter 12(6):607–616. https://doi.org/ 10.1007/s10035-010-0202-y
- Franks NR, Worley A, Falkenberg M, et al (2019) Digging the optimum pit: antlions, spirals and spontaneous stratification. Proceeings of the royal society 286



- Frost JD, Martinez A, Mallet SD, et al (2017) Intersection of modern soil mechanics with ants and roots. In: Geotechnical frontiers 2017 GSP 280 900, pp 900–909
- Girsang CH (2000) A numerical investigation of the seismic response of the aggregate pier foundation system. PhD thesis, Virginia polytechnic institute and state university, http://hdl.han dle.net/10919/36363
- Gregory PJ (2006) Roots, rhizosphere and soil: the route to a better understanding of soil science? Eur J Soil Sci 57(1):2–12. https://doi.org/10.1111/j.1365-2389.2005.00778.x
- Hamza O, Bengough A, Bransby M, et al (2007) Mechanics of root-pullout from soil: A novel image and stress analysis procedure. Eco-and ground bio-engineering: the use of vegetation to improve slope stability pp 213–221. https://doi.org/10.1007/978-1-4020-5593-5_20
- Hu M, Wu B, Zhou W et al (2022) Self-driving shield: intelligent systems, methodologies, and practice. Autom Constr 139(January):104,326. https://doi.org/10.1016/j.autcon.2022.104326
- Huang H, Wu S, Cohen-Or D et al (2013) L1-medial skeleton of point cloud. ACM Trans Graph 32(4):65-1
- JAKY J (1944) The coefficient of earth pressure at rest. Journal of the society of hungarian architects and engineers pp 355–358. https://cir.nii.ac.jp/crid/1571698599493336320.bib?lang=en
- Jarast P, Ghayoomi M (2018) Numerical modeling of cone penetration test in unsaturated sand inside a calibration chamber. Int J Geomech. https://doi.org/10.1061/(asce)gm.1943-5622. 0001052
- 21. Jin W, Aufrecht J, Patino-Ramirez F et al (2020) Modeling root system growth around obstacles. Sci Rep 10(1):1–16
- Kondoh M (1968) Bioeconomic studies on the colony of an ant species Formica Japonica Motschulsky;
 Nest structure and seasonal change of the colony members. Ecol Soc Jpn 18(3):124–133. https://doi.org/10.18960/seitai.18.3_124
- Liu Q, Li J, Liu J (2017) ParaView visualization of Abaqus output on the mechanical deformation of complex microstructures. Comput Geosci 99(June 2016):135–144. https://doi.org/10.1016/j.cageo.2016.11.008
- 24. de Macedo RB, Ando E, Joy S, et al (2021) Unearthing real-time 3D ant tunneling mechanics. In: National academy of sciences, pp 1–7, https://doi.org/10.1073/pnas.2102267118/-/DCSupple mental.y
- Mallet SD, Frost JD, Huntoon JA (2021) Root-inspired anchorage systems for uplift and lateral force resistance seth. In: IFCEE, Ddl, pp 299–307
- Martinez A (2021) Skin friction directionality in monotonicallyand cyclically-loaded bio-inspired piles in sand. DFI J Deep Found Inst. https://doi.org/10.37308/dfijnl.20200831.222
- Martinez A, Palumbo S, Todd BD (2019) Bioinspiration for anisotropic load transfer at soil-structure interfaces. J Geotech Geoenviron Eng. https://doi.org/10.1061/(asce)gt.1943-5606. 0002138
- Martinez A, DeJong J, Akin I et al (2022) Bio-inspired geotechnical engineering: principles, current work, opportunities and challenges. Géotechnique 72(8):687–705
- Monaenkova D, Gravish N, Rodriguez G et al (2015) Behavioral and mechanical determinants of collective subsurface nest excavation. J Exp Biol 218(9):1295–1305. https://doi.org/10.1242/jeb. 113795
- 30. Muir Wood AM (1994) The thames tunnel 1825-43: where shield tunnelling began. Proc Inst Civil Eng Civil Eng 108(2):130–139. https://doi.org/10.1680/icien.1995.27532
- 31. Naclerio ND, Hubicki CM, Aydin YO, et al (2018) Soft robotic burrowing device with tip-extension and granular fluidization.

- IEEE international conference on intelligent robots and systems pp 5918–5923. https://doi.org/10.1109/IROS.2018.8593530
- Öberg AL, Sällfors G (1997) Determination of shear strength parameters of unsaturated silts and sands based on the water retention curve. Geotech Test J 20(1):40. https://doi.org/10.1520/ gtj11419j
- 33. Obrzud RF, Truty A (2018) The hardening soil model–a practical guidebook. Zace Services Ltd. Softw Eng 05:205
- O'Hara KB, Martinez A (2020) Monotonic and cyclic frictional resistance directionality in snakeskin-inspired surfaces and piles.
 J Geotech Geoenviron Eng 146(11):1–15. https://doi.org/10. 1061/(asce)gt.1943-5606.0002368
- Patino-Ramirez F, Anselmucci F, Andò E, et al (2021) Deformation and failure mechanisms of granular soil around pressurised shallow cavities. Géotechnique pp 1–16
- Sadeghi A, Tonazzini A, Popova L, et al (2014) A novel growing device inspired by plant root soil penetration behaviors. PLOS ONE
- Sharpe SS, Kuckuk R, Goldman DI (2015) Controlled preparation of wet granular media reveals limits to lizard burial ability. Phys Biol. https://doi.org/10.1088/1478-3975/12/4/046009
- Soga K (2011) Infrastructure, Springer Netherlands, Dordrecht, pp 59–74. https://doi.org/10.1007/978-94-007-0470-1_4
- Stutz HH, Martinez A, Heepe L et al (2019) Strength anisotropy at soil-structure interfaces with snake skin inspired structural surfaces. E3S Web of Conferences 92:1–6. https://doi.org/10. 1051/e3sconf/20199213008
- Talbot M (1964) Nest structure and flights of the ant Formica obscuriventris Mayr. Anim Behav 12(1):154–158. https://doi.org/ 10.1016/0003-3472(64)90116-2
- 41. TRUEMAN ER (1970) The mechanism of burrowing of the Mole Crab, Emerita. J Exp Biol 53(3):701–710. https://doi.org/10.1242/jeb.53.3.701
- Tschinkel WR (2004) The nest architecture of the Florida harvester ant, Pogonomyrmex badius. J Insect Sci. https://doi.org/10.1093/jis/4.1.21
- Tschinkel WR (2010) Methods for casting subterranean ant nests.
 J Insect Sci 10(88):1–18. https://doi.org/10.1673/031.010.8801
- Tschinkel WR (2021) Ant architecture: the wonder, beauty, and science of underground nests. Princeton University Press, http:// www.jstor.org/stable/j.ctv1bhg2qp
- Tuculescu R, Topoff H, Wolfe S (1975) Mechanisms of pit construction by antlion larvae 1,2. Ann Entomol Soc Am 68(4):719–720. https://doi.org/10.1093/aesa/68.4.719,
- USDA (2019) Web Soil Survey Home. https://websoilsurvey. nrcs.usda.gov/app/
- Tang Y, Huan S, Tao J (2020) Geo-Congress 2020 GSP 320 121.
 In: Asce, Karol 2003, pp 121–131
- 48. Yamamoto K, Vangla P, Frost J (2019) 2d and 3d laboratory studies to understand tunneling behavior of pogonomyrmex occidentalis in different soil conditions. In: Integrative and comparative biology, Oxford Univ Press Inc Journals Dept, 2001 Evans Rd, Cary, NC 27513 USA, pp E256–E256

Publisher's Note Springer Nature remains neutral with regard to jurisdictional claims in published maps and institutional affiliations.

Springer Nature or its licensor (e.g. a society or other partner) holds exclusive rights to this article under a publishing agreement with the author(s) or other rightsholder(s); author self-archiving of the accepted manuscript version of this article is solely governed by the terms of such publishing agreement and applicable law.

